Intrinsically disordered peptides enhance regenerative capacities of bone composite xenografts

Maryam Rahmati [1], Sabine Stötzel [2], Thaqif El Khassawna [2,3], Chenyi Mao [4], Adilijiang Ali [4], Joshua C. Vaughan [4,5], Kamila Iskhahova [6], D.C. Florian Wieland [6], Antonio Gonzalez Cantalapiedra [7,8], Giuseppe Perale [9,10,11], Felice Betge [9], Eoghan P. Dillon [12], Ståle Petter Lyngstadaas [1], Håvard Jostein Haugen [1,*]

[1] Department of Biomaterials, Institute for Clinical Dentistry, University of Oslo, PO Box 1109 Blindern, NO-0317 Oslo, Norway
[2] Experimental Trauma Surgery, Justus-Liebig University Giessen, Giessen, Germany
[3] Faculty of Health Sciences, University of Applied Sciences, Giessen, Germany
[4] Department of Chemistry, University of Washington, Seattle, WA, USA
[5] Department of Physiology and Biophysics, University of Washington, Seattle, WA, USA
[6] Institute of Metallic Biomaterials, Helmholtz Zentrum Hereon, Max-Planck-Straße 1, 21502 Geesthacht, Germany
[7] Universidade de Santiago de Compostela Facultad de Veterinaria: Campus Universitario, s/n, 27002 Lugo, Spain
[8] iBoneLab S.L. Avda. Da Coruña, 500 (CEI-NODUS), 27003 Lugo, Spain
[9] Industrie Biomediche Insubri SA, Via Cantonale 67, 6805 Mezzovico-Vira, Switzerland
[10] Faculty of Biomedical Sciences, Università della Svizzera Italiana (USI), Via G. Buffi 13, Lugano 6900, Switzerland
[11] Ludwig Boltzmann Institute for Experimental and Clinical Traumatology, Donaueschingenstrasse 13, 1200 Vienna, Austria
[12] Photothermal Spectroscopy Corp, Santa Barbara, CA 93101, USA

Biomaterial scientists design organic bone substitutes based on the biochemical properties of the mimicked tissue to achieve near native functionality. Several non-collagenous proteins in bone are known as intrinsically disordered proteins (IDPs), as they lack detectible ordered domains and a fixed 3D structure under physiological conditions. Many IDPs perform regulatory roles in a range of cellular functions, which motivated us to design two proline-rich disordered peptides (P2 and P6) and augmented them into the SmartBone® (SBN) biohybrid substitute. Recently we reported an improved proliferation and osteogensis of human osteoblasts and mesenchymal stem cells in the composite groups containing peptides (named here as SBN + P2 and SBN + P6) *in vitro*. To address the effects of these composites on bone formation and biomineralization, this *in vivo* study investigated their functions in critical size craniotomy defects in 16 domestic pigs after 8 and 16 weeks of healing. For this purpose, we used cone beam computed tomography (CBCT), microCT (μCT), histology, immunohistochemistry, fluorescent labeling of abundant reactive entities (FLARE), synchrotron SAXS/XRD, optical photothermal IR (O-PTIR) microscopy and nanoscale atomic force microscopy-infrared (AFM-IR) analyses. Our results represent new synthetic IDPs as potential candidates for directing bone formation and biomineralization. The SBN + P6 stimulated significantly higher bone formation and biomineralization after 8 weeks of healing compared to other groups indicating its potential in stimulating early biomineralization. After 16 weeks of healing, the SBN + P2 induced significantly

* Corresponding author.
E-mail address: Haugen, H.J. (h.j.haugen@odont.uio.no)

https://doi.org/10.1016/j.mattod.2021.12.001

higher bone formation and biomineralization compared to other groups indicating its effects on later bone formation and biomineralization processes. The vigorous stretching of amide primary and secondary IR absorbance peaks at 1660 and 1546 cm^{-1} in the SBN + P2 group verified that this peptide experienced more conformational changes after 16 weeks of implantation with a higher phosphate intensity at 1037 cm^{-1} compared to peptide 6. Overall, P2 and P6 are promising candidates for bone augmentation strategies in critical clinical applications. We concluded that FLARE and O-PTIR are promising tools in evaluating and diagnosing the biochemical structure of bone tissue and the bone-biomaterial interface.

Keywords: Intrinsically Disordered Proteins; Proline-rich motifs; Bone regeneration; Bone graft substitute; Biomineralization

Introduction

Bone tissue is made up of substances with unique physicochemical properties arranged in hierarchical structures that direct and modulates mineral deposition at the organic-mineral interface [1–3]. Bone extracellular matrix (ECM) is secreted by bone-forming cells and contains collagens and non-collagenous proteins [1–3]. These proteins play fundamental roles in bone mineralization as they modulate crystal nucleation and growth [4]. Several non-collagenous proteins in bone are known as intrinsically disordered proteins (IDPs), as they lack detectable ordered domains and a fixed 3D structure in solutions under physiological conditions [5–7]. These proteins are characterized by their relatively high proportion of charged/polar residues, low sequence complexity and low amount of hydrophobic residues, which can change protein solubility and conformational states [5,8]. IDPs play a key role in directing molecular and cellular signaling pathways such as regulating transcription, translation and cell cycle [9,10]. Because of their regulatory role in cell functions, IDPs are involved in intermolecular interactions of biomineralization processes [11,12]. Therefore, IDPs can adapt to several binding configurations due to their one-to-many and many-to-one signaling capacities [5]. For instance, when interacting with enamel crystals, amelogenin undergoes a conformational change from disordered random coils into ordered β-sheet structures. The conformational change in this disordered protein is responsible for modulating the crystal growth during enamel mineralization [7,12]. In addition, as key players in crystal growth and biomineralization, dentin sialophosphoprotein (DSPP), osteopontin (OPN) and bone sialoprotein-2 (BSP) have disordered structures [13–15]. Hence, it is suggested that synthetic IDPs can be utilized to direct bone formation in bone xenografts via improving their osteoinductivity and osteoconductivity [6].

On the other hand, several ECM proteins (such as collagens, amelogenins, ameloblastin and sialoproteins) involved in biomineralization contain proline-rich regions, suggesting that these regions might bind to hydroxyapatite and calcium ions [16,17]. Proline-rich proteins with dynamic and semi-flexible structures might function as mineral-binding domains, protein–protein interaction domains, or internal molecular parts during the biomineralization process [16,17]. For example, amelogenin and ameloblastin, two major enamel matrix proteins, have a high proportion of poly-proline regions, indicating the importance of proline amino acids in enamel biomineralization [18]. Proline-rich motifs affect the assembly of the ECM proteins and the formation of polyproline II helices. These motifs are therefore linked to the final apatite crystal length in mature enamel [17]. In addition, due to their structural and chemical properties, such regions have high structural selectivity and binding affinity toward a target [19].

Based on these observations, we previously designed a library of synthetic proline-rich IDPs (named Px) to study their effects on biomineralization [20]. In one study, Rubert et al. [17] used three Px (P1, P2, and P3) and studied their effects on the osteoblastic differentiation of MC3T3-E1 and human umbilical cord mesenchymal stem cells (hUCMSCs) [17]. Their results revealed that synthetic peptides have lower cytotoxicity effects on both cell types compared to the commercially available enamel matrix derivative (EMD), Emdogain® (Straumann, Basel, Switzerland). Moreover, cells treated with P2 showed a higher expression of osteoblast marker genes as well as a higher calcium deposition rate compared to EMD and control groups [17]. In another study, Ramis et al. [21] studied the influence of three different Px (P2, P4, and P6) on the osteoblast differentiation of hUCMSCs, either with or without osteogenic supplements (hydrocortisone, b-glycerol phosphate, and ascorbic acid) and compared these to EMD [21]. They assessed the osteoinductivity and biomineralization potential of the groups after 1, 7 and 14 days. Their results suggested that EMD treatment in combination with osteogenic supplements has an immediate and short-lived effect on the osteogenic differentiation of hUCMSCs. In contrast, the designed synthetic peptides combined with osteogenic supplements sustain cell differentiation and biomineralization over a significantly, more extended time [21].

Among different biodegradable materials, animal-derived bone graft substitutes (known as xenografts) have attracted substantial attention as potential candidates for the reconstruction of cranial bone defects during childhood growth [22,23]. Although bovine-derived cancellous bone grafts are the most established xenografts on the market, their osteoinductivity and osteoconductivity need to be improved to achieve a faster regeneration process [24,25]. As proline-rich IDPs seem to have potential functions in modulating the molecular and cellular interactions during bone formation, we incorporated the two most promising synthetic IDPs (P2 and P6) into a xeno-hybrid bone graft, marketed as SmartBone® (SBN) to study their influence on the *in vivo* bone healing and growth. Previous *in vitro*

studies showed that these composites have a bone-positive effect on human osteoblasts and human bone-marrow derived mesenchymal stem cells [26,27].

To investigate the potential of proline-rich IDPs in skull-bone reconstruction, we studied the *in vivo* effects of SBN + P2 and SBN + P6 in a randomized, controlled study in critical size craniotomy defects in 16 young pigs. The observation times after surgical reconstruction of the skulls were 8 and 16 weeks. The long-term goal of the research is to provide safe, biofunctionalized composite bone graft substitutes for bone traumas in challenging bone reconstructions. We hypothesized that encapsulating IDPs into SBN will enhance its osteoinductivity and osteoconductivity by increasing the bone anabolism. We hypothesized that these composites will have a better emergence with the surrounding bone tissue through the remodeling of the old xenograft and stimulating new bone formation. In addition, because the chemical structures of the developed peptides were very similar to each other, we hypothesized to observe similar regenerative capacities effects after implantation. We expected that after implantation, the scaffold porosity would be invaded by cells; matrix would be formed and then mineralized. Based on these assumptions, we used radiological analyses such as cone beam computed tomography (CBCT) to understand the overall healing status and microCT (μCT) to evaluate the microstructural changes within the scaffold. To investigate matrix integrity as well as mineralization and remodeling changes in the scaffolds after implantation, we used synchrotron small angle X-ray scattering and X-ray diffraction (SAXS/XRD). We also used fluorescent labeling of abundant reactive entities (FLARE), optical photothermal IR (O-PTIR) microscopy, and nanoscale atomic force microscopy-infrared (AFM-IR) as chemical imaging tools for the first time to study the chemical interactions between hydroxyapatite and calcium ions with the implanted scaffolds. We also analyzed the newly formed tissue quality judged by less non-mineralized patches and the orientation of mature bone using SAXS/XRD. Such changes are not purely mechanical and chemical, but are caused by and reflected on the cellular balance and changes, which we analyzed histologically. We studied mineralized versus non-mineralized bone formation using different histological staining and then performed immunohistochemistry (IHC) to investigate anabolic and catabolic activities.

Materials and methods

Molecular dynamic simulation of peptides

We used proline-rich IDPs, P2 and P6 designed by Corticalis AS, Oslo, Norway and supplied by Pepmic Co., Ltd., Jiangsu, China. We created the atomistic models for the peptide sequences with the Biovia Discovery studio (Ver 17.2.0, 3DS Paris Campus, Vélizy-Villacoublay, France). The first simulation used the "OPLS-AA/L" all-atom force field to parameterize the peptides. The initially extended peptides were immersed in a periodic simulation box filled with water molecules using the TIP3P water model buffered at 30 angstroms [28]. Then, the peptide models were simulated to obtain the equilibrated configuration for the peptides in solution. After preliminary minimization, the model systems were heated for 100 ns in an orthorhombic ensemble molecular dynamic (MD) simulation run to reach the experimental temperature of 27 °C (300 K). During this step, the water molecules were kept fixed. All restraints were then removed, and the peptides were simulated by running 100 ns of an isothermal-isobaric MD simulation at 300 K of temperature and 1 atm of pressure under periodic boundary conditions. To mimic the bone microenvironment, a second simulation was performed with the "OPLSIDPSFF" all-atom force field [29] using the TIP4P-D water model and Phosphate Buffered Saline (PBS) running for 1000 ns. The PBS environment was simulated by randomly placing Ca^{2+}, PO^{4-} and OH^{-} ions forming hydroxyapatite $Ca_5(PO_4)_3$-OH clusters and $15Na^{+}$ ions, $30Cl^{-}$ ions, and $15K^{+}$ ions (Fig. S4). The unique 7.4 pH environment was created by altering the protonation state of titration sites. The pKa values for each protonation site in peptides were predicted using 'Prepare protein wizard' and Schrodinger's Desmond simulation setup modules (Schrödinger, New York, USA). The MD runs used a time step of 2 femtoseconds, the Langevin thermostat, and a 9 Å cutoff. The particle mesh Ewald5 (PME) approach was used to treat the long-range electrostatic effects, and the SHAKE algorithm was used to treat the bonds involving hydrogen atoms. Simulation quality analysis (SQA), simulation event analysis (SEA), and simulation interaction diagram modules of Schrodinger's Desmond package (Schrodinger's Desmond ver 3.6, Schrödinger, New York, USA) were employed to analyze the simulation and to generate the graphs. The MD trajectory files were analyzed using simulation quality analysis (SQA), simulation event analysis (SEA), along with simulation interaction diagram (SID) programs available with the Desmond module. Using these programs, we calculated the peptide's energy, root-mean-square deviation (RMSD), root-mean-square fluctuation (RMSF), total intramolecular hydrogen bonds, radius of gyration (Rg), and secondary structure elements (SSE) of the protein contributing to the structural stability. MolProbity [30] was used to calculate (ϕ,ψ) angles of all residues in the protein structures and classify them as favored, allowed, or outlier at 0, 700 and 1000 ns.

Small-angle X-ray scattering (SAXS) and circular dichroism (CD) analyses of peptide's structure

We studied the disordered manner of peptides using both SAXS and CD analyses. A total of 0.1 mg/mL of P2 and P6 were dissolved in 10 mM sodium phosphate buffer, and were measured at pH 7.4. Here we present the Kratky plot that plots the scattering pattern as q^2 I(q) versus q. The Kratky plot is a valuable tool to determine disorder behavior in peptides and proteins.

The circular dichroism (CD) measurements were performed using a Chirascan from Photophysics. The samples were measured with a concentration of 0.1 mg/mL using a 10 mM PBS buffer at a pH value of 7.4. The CD spectra were performed in the wavelength range from 180 to 280 nm with a step width of 0.5 nm with 0.5 s per point. Three spectra were measured and averaged afterward. Just before the measurement, a cuvette with the buffer was measured and subtracted as background.

Scaffold design

The commercially available xeno-hybrid bone graft SmartBone® (SBN, manufactured by Industrie Biomediche Insubri SA, IBI SA, Mezzovico-Vira, Switzerland) was used in this study, which consists of a bovine bone-derived mineral matrix improved by the

reinforcement with the co-polymer coating poly(L-lactide-co-ε-caprolactone) (PLCL) and the addition of RGD-exposing collagen fragments from animal-derived gelatin. The manufacturing process of SBN is described in detail in previous studies [31,32].

During the standard manufacturing process of SBN, P2 and P6 were encapsulated into the PLCL coating layer of SBN to produce SBN + P2 and SBN + P6. Before designing the scaffolds, peptides were prepared as stock solutions at 4 mM in 0.1% acetic acid and stored at −20 °C. Perale et al. [33] studied the release profiles, cytotoxicity, morphology, and mechanical strength of scaffolds. The release rate of peptides was 1 $\mu g/cm^3/d$ over two weeks [33].

Disc shape scaffolds with a height of 4 mm and a diameter of 16 mm were produced for this *in vivo* study. All manufacturing batches were released following the same SBN standard release procedures, under c-GMP and ISO13485–2016 compliance (by Industrie Biomediche Insubri SA, Mezzovico-Vira, Switzerland).

Animal surgery

A total of 16 hybrid pigs, 8 per time point (Breeding farm, Spain) (age: 3–4 months, quarantine period: 21 days) were used for this study. All the experiments were carried out according to the national legislation following the community guidelines after the authorization of the competent autonomous authority in the facilities available to the Rof Codina Foundation for this purpose (Approval number: AE-LU-001). The animals were kept as a group in an area with natural light, air renewal and regulated temperature. Animals were fed using a specific granular diet for their species and free water supply. All procedures were performed using general anesthesia induced with propofol (2–4 mg/kg/i.v., Propovet, Abbott Laboratories, Kent, UK) and maintained with iso/sevoflurane (Isoba-vet, Schering-Plow, Madrid, Spain). Previously, the animals were medicated with ketamine (10 mg/kg/i.m.), midazolam (0.5 mg/kg/i.m.), morphine (0.5 mg/kg/i.m.) and meloxicam (0.2 mg/kg/i.m.) for pain control under veterinary care. During anesthesia, the animals were monitored via electrocardiography, capnography, and pulse oximetry as well as non-invasive blood pressure. The animals were monitored daily and during the interventions by a veterinarian accredited and trained in the science of laboratory animals (categories B or C, functions a, b and c).

For the detailed surgical procedure, a longitudinal incision was made at the level of frontal bone, and the muscles were reflected. Then, four perforations (with a diameter of 16 mm and a depth of 4 mm) were made at the level of the frontal and parietal bones under continuous irrigation with sterile saline. The samples were then implanted in the defect site. All defects except sham were covered with a bovine pericardium membrane (Tutopatch, Tissue Matrix, Tutogen Medical GmbH, Germany) and immobilized with five titanium screws, which were also important for accurate guidance of later micro-CT and histology analyses (Fig. S1). Muscular, subcutaneous, and skin tissues were then gently closed. Antibiotic prophylaxis was administered for a period of one week using amoxicillin (20 mg/kg/s.i.d./s.c.).

Cone beam computer tomography (CBCT) images were obtained on the 8th and 16th week (3D-Exam scanner, KaVo Dental, Biberich, Germany). For the scanning procedure, the pigs were positioned on the supporting plate provided by the manufacturer and positioned in the center of field of view (FOV) using the laser orientation beams. Scans were obtained with the following technical parameters: 120 kV acceleration voltage, 5 mA beam current, FOV a diameter of 16 cm, FOV height of 6 cm, 600 projections, 360° rotation, voxel size of 0.3 mm, and scanning time of 9 s. The 3D images were generated in RadiAnt DICOM Viewer (Medixant, Poznań, Poland).

Animals were sedated and then sacrificed by an overdose of pentobarbital (40–60 mg/kg/i.v.) After 8 or 16 weeks of healing. The explanted bone blocks with the bone defects were dissected from soft tissues, fixed in phosphate-buffered 4% paraformaldehyde and kept at 4 °C until processing.

μCT 3D analyses

The fixed bone defects were scanned in a μCT system (Bruker microCT2242, Kontich, Belgium) with the scanning parameters set at 104 μA, 95 kV, image rotation of 0.4 degrees, a resolution of 7.9 μm, and a 1 mm aluminum copper filter. After reconstruction, the region of interest (ROI) was relocated with the guidance of previously implanted titanium screws (Fig. S2). A cylindrical ROI of 16 mm in diameter and 4 mm in thickness was made in each sample for quantification. Morphometrically parameters as bone volume ratio (Obj.V/TV), bone surface/volume ratio (Obj.S/Obj.V) and bone surface density (Obj.S/TV) were analyzed by CTan (Bruker microCT, Kontich, Belgium). 3D images were rendered with CTVox.

Histology and immunohistomochemistry analyses

After μCT imaging, we cut samples in half to study bone formation and biomineralization in both calcified and decalcified bone tissues. Half of the defect site was embedded in methyl methacrylate (MMA) to preserve the calcified tissue. The other half was decalcified using ethylenediaminetetraacetic acid (EDTA) 10% for four months and then embedded in paraffin. The paraffin samples (eight samples per group) were cut cross-sectional to the medial plane of the animal body in 5 μm thickness (Fig. S3). Because of the procedure difficulties, three MMA embedded samples were randomly chosen and sectioned in 5 μm thickness onto Kawamoto's film (SECTION-LAB Co. Ltd., Hiroshima, Japan), longitudinal to the pig medial plane. As described in previous papers, Movat Pentachrome and Von Kossa/Van Gieson stains were used to evaluate the bone mineralization/non-mineralization balance over time [34,35]. Alkaline phosphatase (ALP) and tartrate-resistant acid phosphatase (TRAP) enzyme histochemistry were done to study the osteoblast and osteoclast balance [36,37]. Collagen fibers properties (such as width, length, straightness and angle) were evaluated using Sirius Red.

Immunohistochemistry was performed using primary antibodies (Abcam Company, Cambridge, UK). The following antibodies were used: rabbit monoclonal (EPR53) to alpha-smooth muscle Actin (α-SMA), rabbit monoclonal (EPR14334) to runt-related transcription factor 2 (Runx 2), rabbit polyclonal (OAA100188) to osteopontin, mouse monoclonal (LS-C83497-100) to osteocalcin and rabbit monoclonal (EPR7785) to collagen type I. Readers can find the details of immunohistochemistry protocol and materials elsewhere [38].

To study the blood vessel formation, α-SMA was diluted in DAKO-Diluent (S 0809), 1:1000. Regarding bone formation in calcified sections, osteopontin, osteocalcin and collagen type I were diluted in DAKO-Diluent, 1:250, 1:800 and 1:2000, respectively. Runx 2 was diluted in DAKO-Diluent (1:500) to study the bone formation in decalcified sections. Goat anti-rabbit (BA-1000, Vector) and methyl green staining were used as the secondary antibody and counterstain, respectively.

We chose decalcified Movat Pentachrome and calcified α-SMA stained sections to study the general tissue formation descriptively. In the Movat Pentachrome stained sections, we studied the tissue homogeneity and integrity as well as defect closure in all groups using a 3-point scale system (poor, fair, good for 1 to 3, respectively) by two independent and calibratated examiners. Additionally, α-SMA stained sections were used to study the blood vessel phenotype and regularity over time using a 3-point scale system. We defined the round shape vessels as regular type 1, small to moderate oval shape ones as regular type 2 and big vessels in oval or other undefined shapes as irregular type 3 vessels.

Fluorescent labeling of abundant reactive entities (FLARE) analysis

Samples embedded in MMA were sliced into 5 μm sections and the sections were labeled using a modified FLARE stain protocol [39] to stain oxidized carbohydrates and primary amines (proteins, chiefly). We first soaked sections in 2-methoxyethyl acetate (Millipore Sigma, 806061) for 30 min to dissolve MMA and then we rehydrated the sections in a series of ethanol/water mixtures that have descending ethanol concentrations (100%, 90%, 70%, 50%, 30%, 0%), with 5 min per rehydration solution. The carbohydrate stain consisted of a 30 min oxidation step with freshly prepared 50 mM $NaIO_4$ (Millipore Sigma, 311448) in 100 mM sodium acetate pH 5 to oxidize carbohydrates to aldehydes, washing with 100 mM sodium acetate pH 5 three times for 5 min each, reacting for two hours with 2.5 μg/mL Alexa Fluor 568-hydrazide (ThermoFIsher, A10437) in 100 mM sodium acetate pH 5 to conjugate the dye to the aldehyde groups, 30 min reduction with a freshly prepared 5 M $NaCNBH_3$ (Millipore Sigma 156159) in 100 mM sodium acetate pH 5 to stabilize the dye linkages (converting hydrazone groups to stabler secondary amines), and washing with 100 mM sodium acetate pH 5. The primary amine (protein) stain was performed by incubating sections with 2.5 μg/mL ATTO 647N-NHS ester dye (Sigma Aldrich, 18373) in PBS for 30 min and then washing the sections with PBS three times. Sections were imaged using two modalities. We used a 4× objective lens on a wide-field fluorescence microscope to tile the entire region and then used a 20× objective lens and 60× water immersion objective lens on a confocal microscope (Leica SP5 II) to image regions of interest at higher resolutions. The free software package ImageJ was used for image visualization, merging of channels, and image registration.

Quantitative histomorphometry analysis

Imaging was performed using an automated slide scanner system (Axio Scan Z1, Carl Zeiss Microscopy, Munich, Germany) for all stained sections (except TRAP and Sirius Red) at 20× magnification. Sections stained with Sirius Red and TRAP were imaged at 40× magnification using a Leica microscopy system (Leica DM5500 photomicroscope equipped with a DFC7000 camera and operated by LASX software version 3.0, Leica Microsystem Ltd, Wetzlar, Germany). The histomorphometry measurements of Sirius Red stained sections were performed using CT-FIRE (Curvelet Transform and Fiber Extraction Algorithm) software developed in MATLAB [40]. Fiji (version 1.51r; NIH, Maryland, USA) was used for histomorphometry measurements of other stained sections. The histomorphometry measurements were done following Malhan et al. [41] method to analyze tissue formation parameters such as mineralization, new bone and cartilage formation as well as vascularization.

Small-angle X-ray scattering/X-ray diffraction (SAXS/XRD) analysis

We used calcified bone sections with 70 μm thickness to study the collagen/hydroxyapatite (HAp) orientation and size of hydroxyapatite plates using SAXS/XRD analysis. We performed SAXS/XRD scanning at the synchrotron beamline P12, Petra III, Deutsches Elektronen-Synchrotron (DESY) Hamburg, operated by the European Molecular Biology Laboratory (EMBL). The used photon energy was 18 keV, and the beam size was determined to be 80 μm by 80 μm. The sample to detector distance was 1.5 m. We used a Pilatus 6 M Detector, Dectris, Switzerland, with a pixel size of 172 μm. The exposure time of one second was used. Due to the energy settings, the short sample to detector distance, and the large detector, it was possible to record the SAXS and XRD signal on one detector simultaneously. Data averaging and reduction were made by the EMBL analysis pipeline. We used a mesh scan with a stepping 0.15 mm perpendicular and 10 mm parallel to the sample. The total size of the scanned area was adjusted to the respective sample size.

We evaluated the hydroxyapatite platelets' parameter and orientation (HAp) data using in-house written MATLAB® scripts. For evaluating the T parameter, we used the stack and card model developed by Gourrier et al. [42] and adjusted them to the data. T parameter is the measurement of HAp platelet size and indicates the HAp platelet thickness [42].

Optical photothermal IR (O-PTIR) analysis

We used a mIRage IR + Raman microscope (Photothermal Spectroscopy Corp.) to collect optical photothermal infrared (O-PTIR) absorbance spectra. The spectra were collected with simultaneous co-localized Raman scattering spectra using a Schwarzschild-type Cassegrain reflective objective (Numerical Aperture: 40 × 0.78, Working Distance: 8.3 mm, Field of View: 165 μm × 125 μm) microscope system to focus both 532 nm and IR laser light, in a colinear fashion, to the same location. The mIRage IR + Raman microscope uses a 1–200 mW continuous wave 532 nm diodepumped solid-state laser as a probe light, while a tunable pulsed quantum cascade laser (QCL) with a repetition rate of 100 kHz and pulse widths between 40–500 ns with a spectral resolution of 2 cm^{-1} was used to excite the sample selectively. We collected the simultaneous Raman spectra in back-reflected light through the Cassegrain objective using a Horiba iHR320 with a spectral resolution of 4 cm^{-1}. We obtained

discrete single-frequency IR amplitude images by scanning a selected area within the view field of objective at stage step-size of 100 nm. We used O-PTIR Studio software to process IR amplitude ratio images and IR spectral data. All spectral data were collected under ambient conditions with minimal sample preparation.

Nanoscale atomic force microscopy-infrared (AFM-IR) analysis

We collected the location-specific deflection photothermal IR spectra with nanolateral spatial resolution using a nanoIR system (Bruker Corporation). The nanoIR system uses a tunable pulsed optical parametric oscillator as a mid-IR source 5 and a visible continuous wave laser reflective atop of an AFM cantilever of length 150 μm, tip height 10 μm, and a tip radius of 10 nm. We did one spectrum per imaging point (with at least 7 spectra per sample) and used a slight Savitzky-Golay-Filter (2 sidepoints, 3rd order). The data were smoothed using 13 sidepoints for the moving regression window of the polynomial. All spectra used for averaging represent a single spectral acquisition at each individual lateral position (no multiple ones). For averaging, all used spectra were normalized (same data average and data span). For the display of several spectra in one graph, the respective single spectra, groups, or averages were offset to visualize the differences more clearly.

Statistical analysis

A Shapiro–Wilk was used as a normality test. When the data were distributed normally, they were presented as arithmetic mean values with standard deviation, and when the data were not normally distributed, they were presented as median values with the interquartile range. Two-way ANOVA on ranks was performed when the normality test failed, using the Kruskal–Wallis test for post hoc comparison. Otherwise, regular ANOVA was performed with a Tukey test for post hoc comparison. All analyses were performed in GraphPad Prism 8 (GraphPad Software Company, San Diego, CA). Significant differences were presented as *$P < 0.05$ and **$P < 0.01$,* ***$P < 0.001$ and ****$P < 0.0001$.

Results

Molecular simulation and structure of peptides

The sequence of P2 and P6 is shown in Table S1. Both peptides had polar and hydrophobic amino acids; however, there were few differences in the type of amino acids. P2 had serine and glutamine as polar amino acids, while P6 had histidine and glutamine. In addition, methionine as a hydrophobic amino acid was only present in P6. The MD simulations revealed that both peptides had a rather dynamic behavior in solution (Table S1).

Regarding MD analysis, we first confirmed that the overall simulation was carried out at the same temperature, volume and pressure for both peptides by running SQA under both OPLS-AA/L-TIP3P and OPLSIDPSFF-TIP4P-D + PBS conditions (Fig. S5&6). Results indicated that the MD system of both peptides maintained the 300 k temperature; approx. 1 atm pressure and overall volume of the simulation box as 815,000 & 770,000 angstrom cubes with 80,416 and 75,872 total number of atoms. The difference in the simulation box size is due to the initial model structures of P2 & P6, where P2 was more in the stretched state compared to P6 (Fig. 1a–d). Calculated total energy along with potential energy of the OPLS-AA/L-TIP3P simulated system was between −20750 & −255000 Kcal/mol on average for P2 and between –19550 & −241500 on average for P6 during the simulated timescale of 100 ns (Fig. S8A). Whereas, calculated total energy and potential energy of the OPLSIDPSFF-TIP4P–D + PBS simulated system were between −56500 & −67500 Kcal/mol on average for P2 and −58500 & −69500 Kcal/mol on average for P6 after 1000 ns during the simulated timescale of 1000 ns (Fig. S8B). Overall, the average minimized energy of P2 was lower than P6 during the simulated timescale of 1000 ns (Fig. S8). Since the thermo-dynamic structural stability was higher at lower energy levels, we concluded that P2 was more thermodynamically stable than P6, thus more favorable for initiating biomineralization processes. We also measured the total number of intramolecular hydrogen bonds throughout the simulated timescale of 100 & 1000 ns for peptides (Fig. S9). During the simulated timescale of 1000 ns, P2 maintained an average of four intramolecular hydrogen bonds with up to 10 as maximum throughout the simulated timescale, whereas P6 peptide was observed to maintain an average of six intramolecular hydrogen bonds with up to 11 as maximum. In general, more number of intramolecular hydrogen bonds gave a more stable/-rigid structure and decreased the ability to interact with other micro or macromolecules. Therefore, P2 had more flexibility and open residues to interact with other micro- or macromolecules, which was also evident from the least energy snapshots (Fig. 1e&f). To understand the overall impact of the energy on the peptides' structural integrity, we sampled snapshots from the simulation, where peptides had the least energy during the simulated timescale of 100 & 1000 ns (Fig. 1e&f, Figs. S10-12). Visual inspection of the snapshots showed that the folding process of P2 happened faster than P6 during the simulated timescale of 100 & 1000 ns under both simulation conditions (Fig. 1e&f, Figs. S10-12).

From the RMSD analysis (Fig. 1g&j), we observed that P6 is more rigid in its backbone structure, leading to less interactions with other micro/macromolecules or peptides compared to P2 during 100 and 1000 ns simulated timescale. The higher values of RMSD for P2 indicated its spontaneous folding tendency. In addition, we studied the behavior of individual residues as the simulation made progress using RMSF under both conditions (Fig. 1h&K). Peptides were different at their residual level. However, residues numbered 2, 17, 18, 20 & 22 fluctuated with similar frequencies and distance on average under OPLS-AA/L-TIP3P condition. Whereas, under OPLSIDPSFF-TIP4P-D + PBS condition, only residues numbered seven fluctuated with similar frequency and distance on average. The Rg analysis under OPLS-AA/L-TIP3P condition (Fig. 1i) demonstrated that initially, the Rg value for both peptides was about 20 angstroms. This value changed for peptides after 10 ns. While P6 stretched up to 30 angstroms, P2 was spontaneously folded with less than 10 angstroms radius after the initial 20 ns. After crossing about 65 ns, P6 was spontaneously folded with 5 angstroms of radius; whereas, P2 was folded with 15 angstroms radius. The Rg analysis under OPLSIDPSFF-TIP4P-D + PBS condition exhibited that both peptides had an initial Rg of around 20 angstroms. After 180 ns, this value changed to 15 and 10 angstroms for P2 and P6, respectively (Fig. 1l). To further understand this sudden change in the

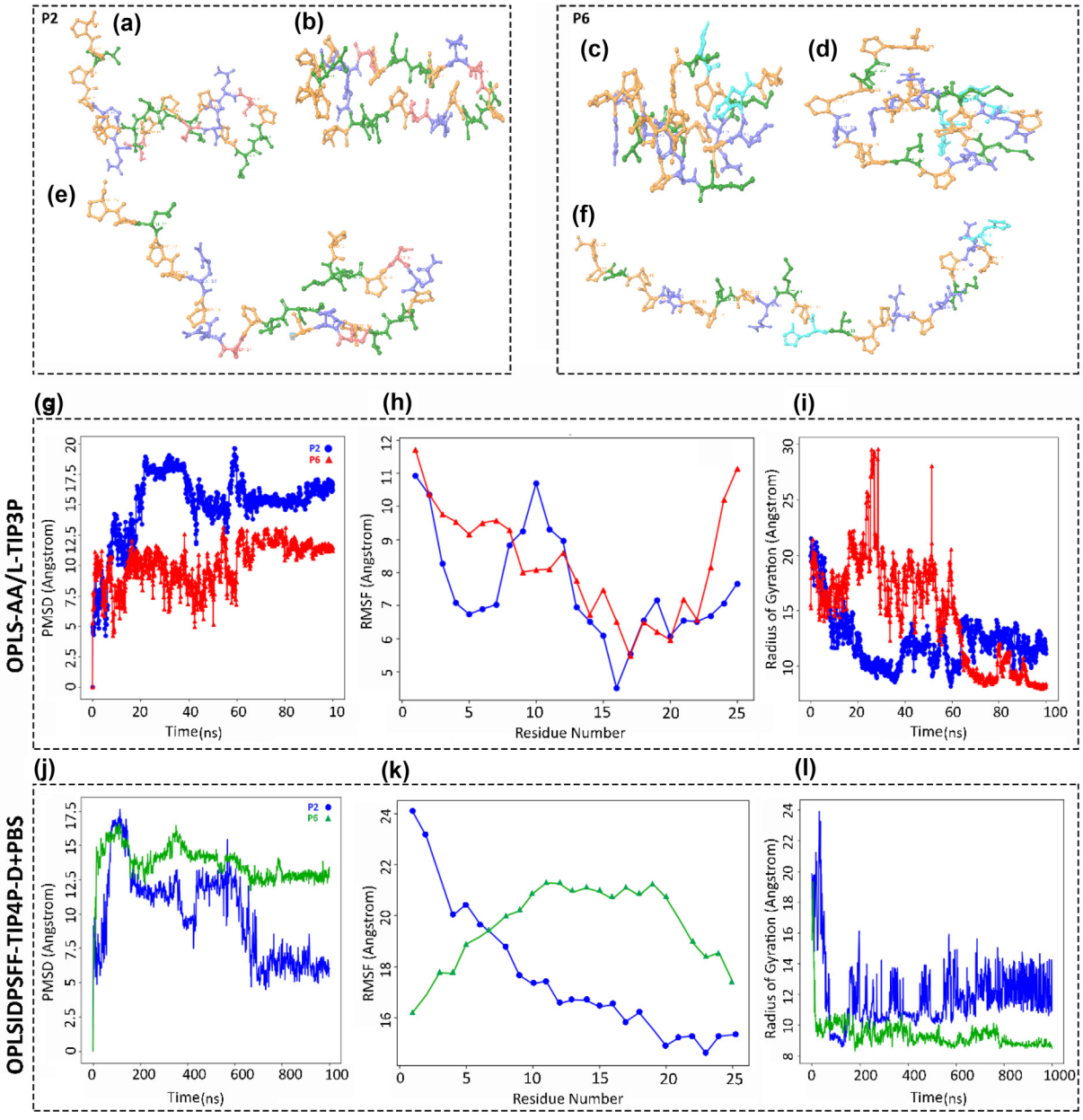

FIGURE 1

Molecular simulation (MD) analysis of peptides' disordered manner. Initial modeled structures of P2 peptide, front view (a) and top view (b). Initial modeled structures of P3 peptide, front view (c) and top view (d). The disordered structure of P2 and P6 from the simulated timescale, where it was shown to have the least minimized energy (e & f). Calculated root-mean-square deviation (RMSD) (g & j), Root Mean Square Fluctuations (RMSF) (h & k) and Radius of Gyration (Rg) (i & l) graphs of P2 and P6 under OPLS-AA/L-TIP3P and OPLSIDP-TIP4P-D + PBS conditions.

Rg, we sampled a simulation snapshot of both peptides at 700th ns and identified that all Ca^{2+}, PO^{4-} and OH^{-} ions formed clusters around the initial five residues noticeably (Fig. S12). Whereas in the case of P6, Na^{+}, Cl^{-} and K^{+} were the major ions that aggolomorated around the hydroxylapatite clusters (Fig. S12).

To mimic the bone environment, we chose the OPLSIDP-TIP4P-D + PBS condition to interpret molecular interactions of P2 with Ca^{2+}, PO^{4-} and OH^{-} ionic clusters. There were 21 contacts between P2 peptide with these ions, out of which eight connections were involved in ionic bonds (Fig. S13). Pro1 residue of P2 interacted with Hydrogen bonds, while Pro1, Ser11, Gln12, Leu14, Ser17, Pro24, and Pro25 residues were involved in the ionic interactions (Fig. S14). Regarding P6, a total of 16 contacts were observed between P6 and Ca^{2+}, PO^{4-} and OH^{-} ionic clusters, out of which four connections were involved in Hydrogen bonds, two contacts in hydrophobic interactions and seven contacts in ionic bonds (Fig. S15). Hydrogen bonds interacted with Pro1, His2, Gln3 and His12 residues, while ionic bonds interacted with Pro1, His2, Gln3, Gln6, His12, and Pro25 residues (Fig. S16). In addition, Ramachandran plots of P2 and P6 in the PBS environment at 0, 700 and 1000 ns simulated timescale was performed (detail shown in Fig. S17).

The Kratky representation allows discrimination between different shapes of proteins [43]. Fig. S18 shows the typical behavior

of used disordered peptides using bioSAXS analysis [44]. In addition, our CD results confirmed the disordered manner of the peptides (Fig. S19).

Bone formation and mineralization

We studied the effects of IDPs on bone formation and mineralization using several techniques. The 3D reconstructed images resulting from CBCT were used to assess the healing progression descriptively. While most defects in the treated groups were fully covered with bone tissue, 5 out of 8 samples in the sham group showed partial cortical bone consolidation (Figs. 2a&S9). The images showed that after 8 weeks of healing, treated groups had higher active bone formation and remodeling compared to the sham. This is consistent with our μCT results showing significantly higher bone volume and surface density after 16 weeks compared to 8 weeks of healing in the treated groups (Fig. 2b&c). Although we could not detect any statistically significant differences between groups regarding their bone volume ratio (Obj.V/TV), our data showed that the Obj.V/TV of the SBN + P2 group was higher than all three other groups at both

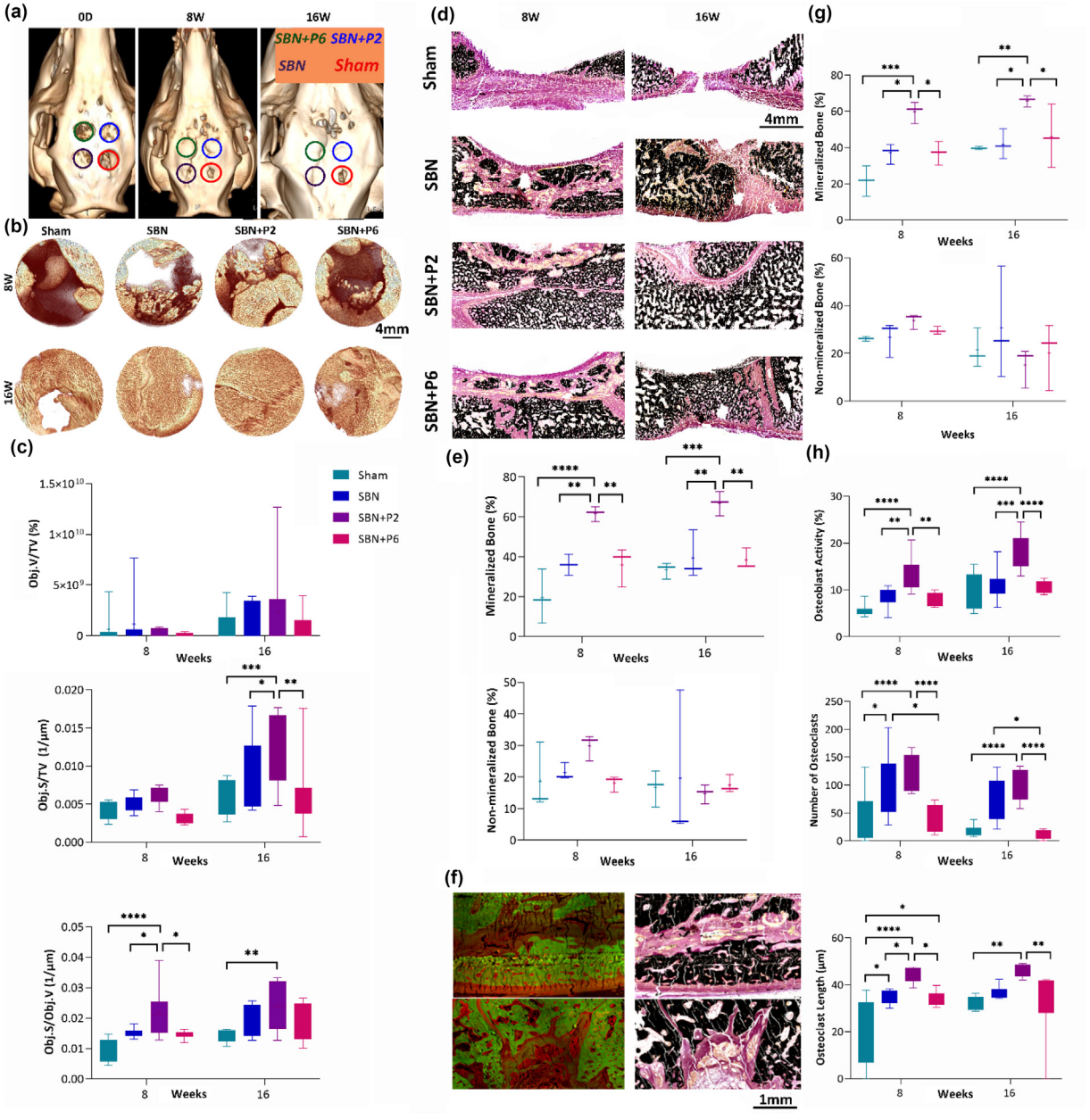

FIGURE 2

Studying osteogenesis and biomineralization effects of proline-rich disordered peptides. (a) Representative images of monitoring bone healing in four groups including sham, SmartBone® (SBN), SBN + P2 and SBN + P6 using cone-beam computed tomography (CBCT) after 8 and 16 weeks of healing, ($N = 8$). (b & c) Representative images and statistical data of μCT analysis of bone volume ratio (Obj.V/TV), bone surface/volume ratio (Obj.S/Obj.V) and bone surface density (Obj.S/TV), scale bar = 4 mm, ($N = 8$). (d–g) Representative images and statistical data of studying mineralized/non-mineralized balance of calcified samples using Von Kossa/Van Gieson histology staining (d & e) and fluorescent labeling of abundant reactive entities (FLARE) analysis, scale bar = 1 mm (f & g), ($N = 3$). (h) Studying osteoblast and osteoclast activities using alkaline phosphatase (ALP) and tartrate-resistant acid phosphatase (TRAP) staining in decalcified samples, respectively ($N = 8$). Significant differences were presented as $^{*}P < 0.05$, $^{**}P < 0.01$, $^{***}P < 0.001$ and $^{****}P < 0.0001$.

time points (Fig. 2c). The sham and SBN + P6 groups had almost the same Obj.V/TV and bone surface density (Obj.S/TV) values. The differences between groups were more noticeable in bone surface/volume ratio (Obj.S/Obj.V) and Obj.S/TV data as the values for the SBN + P2 group were significantly higher than other groups. After 16 weeks of healing, the Obj.S/TV ratio for the SBN + P2 group was significantly higher compared to sham, the SBN and SBN + P6 groups with P values of 0.0002, 0.0499 and 0.0012, respectively. This is in line with the Obj.S/Obj.V results, where the ratio of the SBN + P2 group was significantly higher than that of sham, SBN and SBN + P6 with *P* values of <0.0001, 0.0478 and 0.0251, respectively, after 8 weeks of healing.

After 3D μCT analysis, we studied the mineralized/non-mineralized bone formation of calcified samples using histology stains such as Von Kossa/Van Gieson and Movat Pentachrome, and a recently developed chemical stain called FLARE [39]. Fig. 2d&e shows the results from Von Kossa/Van Gieson staining, which stains the mineralized, newly produced bone matrix and bone marrow in black, pink and brown, respectively. The results confirmed μCT data, showing significantly higher mineralized bone tissue in the SBN + P2 group compared to sham, SBN and SBN + P6 groups with *P* values of <0.0001, 0.0086 and 0.0088, respectively, after 8 weeks of healing. The same pattern is seen after 16 weeks of healing with *P* values of 0.0009, 0.0049 and 0.0037, respectively. There were no significant differences between groups in terms of their newly produced bone matrix formation (shown as non-mineralized bone).

For the FLARE stain, two reactive fluorophores were used to reveal the distribution of carbohydrates and amines, respectively [39]. Using this technique, we detected a distinguishable carbohydrate and amine distribution between the mineralized and non-mineralized regions (Fig. 2f), where the mineralized region is carbohydrate-rich (green) and the non-mineralized region is amine-rich (red). In addition, the labeling pattern regarding the mineralization is correlated with the Von Kossa/Van Gieson histology staining (Fig. 2f). We observed the same pattern regarding mineralized tissue but with lower P values of 0.0002, 0.0208 and 0.0213 for sham, SBN and SBN + P6 groups, respectively after 8 weeks of healing (Fig. 2g). The data for non-mineralized tissue followed the same pattern as Von Kossa/Van Gieson data; however, the values were higher for FLARE, which could be because using this tool, we could not distinguish between bone marrow and newly produced bone matrix as clearly as Von Kossa/Van Gieson staining (Fig. S10). We hypothesized that this could be because of the high amount of amine groups in both the new bone matrix and bone marrow and the conformational changes of P2 from disordered random coils into ordered β sheet structures. In summary, the comparison between data obtained from both histology and FLARE stains indicated the promising applications of FLARE in evaluating bone tissue as a complementary technique for histology. However, developing more stains for targeting different chemical groups and improving its specificity to subsets of proteins or carbohydrates could help to implement this new tool to study the bone tissue chemically.

The percentage of mineralized tissue was also significantly higher for the SBN + P2 group compared to the sham in Movat Pentachrome calcified sections with P values of 0.0273 and 0.0398 at 8 and 16 weeks of healing, respectively (Fig. S11). Movat Pentachrome calcified sections also showed higher insignificant values of non-mineralized bone tissue for the SBN + P2 group after 4 weeks of healing.

We also studied bone formation and absorption rates, using ALP and TRAP enzyme histochemistry (Figs. 2h&S11). In decalcified samples, the osteoblast activity of the SBN + P6 was approximately as same as that of the SBN and higher than that of the sham after 8 weeks of healing. However, there were no distinguishable differences between the sham, SBN and SBN + P6 groups. The SBN + P2 had significantly higher osteoblast activity than that of sham, SBN and SBN + P6, in both time points, with *P* values of <0.0001, 0.0038 and 0.0013, respectively after 8 weeks, as well as <0.0001, 0.001 and <0.0001, respectively after 16 weeks of healing. The osteoclast number and length were significantly more significant in the SBN and SBN + P2 groups than in other groups, indicating higher bone resorption activity. Data obtained from TRAP staining of calcified samples showed the same pattern as decalcified samples (Fig. S11). Comparing osteoblast and osteoclast activities, data exhibited that encapsulating P2 into SBN stimulated significantly higher bone formation and greater bone resorption activities indicating a better bone metabolism balance than other groups. While the bone formation activity of SBN and SBN + P6 was in the same range of sham, the SBN had higher bone resorption rates than that of sham and SBN + P6.

Using Sirius Red staining, we also evaluated the collagen properties of bone tissue in different groups (Fig. S12). Although there were no significant differences between groups regarding their length, angle, and straightness, the sham group fibers were significantly wider than the treated groups. In addition, the fiber angle in the SBN + P2 group was more close to 90 degrees indicating better bone formation than other groups.

Descriptive analysis of bone formation

We also evaluated the percentage of bone mineralized/non-mineralized and cartilage distribution in decalcified samples using Movat Pentachrome staining (Fig. 3a), and the data were consistent with the previous results. The percentage of both mineralized and non-mineralized tissue was higher in all SBN treated groups compared to the sham in both time points (Fig. 3b). The percentage of mineralized tissue was significantly higher for the SBN + P2 group than the sham, SBN and SBN + P6 with *P* values of <0.0001, 0.0001 and 0.0003, respectively after 8 weeks, as well as <0.0001, 0.0021 and <0.0001, respectively after 16 weeks of healing. Although our Von Kossa/Van Gieson and FLARE data showed lower non-mineralized tissue after 16 weeks of healing in the SBN + P2 group compared to others, we observed significantly higher percentage of that in this group, after both 8 and 16 weeks of healing here. While there were no significant differences between groups regarding the percentage of cartilage distribution, the value was higher for SBN + P6 than other groups, indicating the potential ability of P6 in stimulating cartilaginous tissue and early mineralization.

The descriptive analysis of decalcified samples showed that groups with encapsulated peptides had better defect closure and tissue homogeneity compared to the SBN and sham groups after 8 weeks of healing. (Fig. 3c–e). While none of the sham sam-

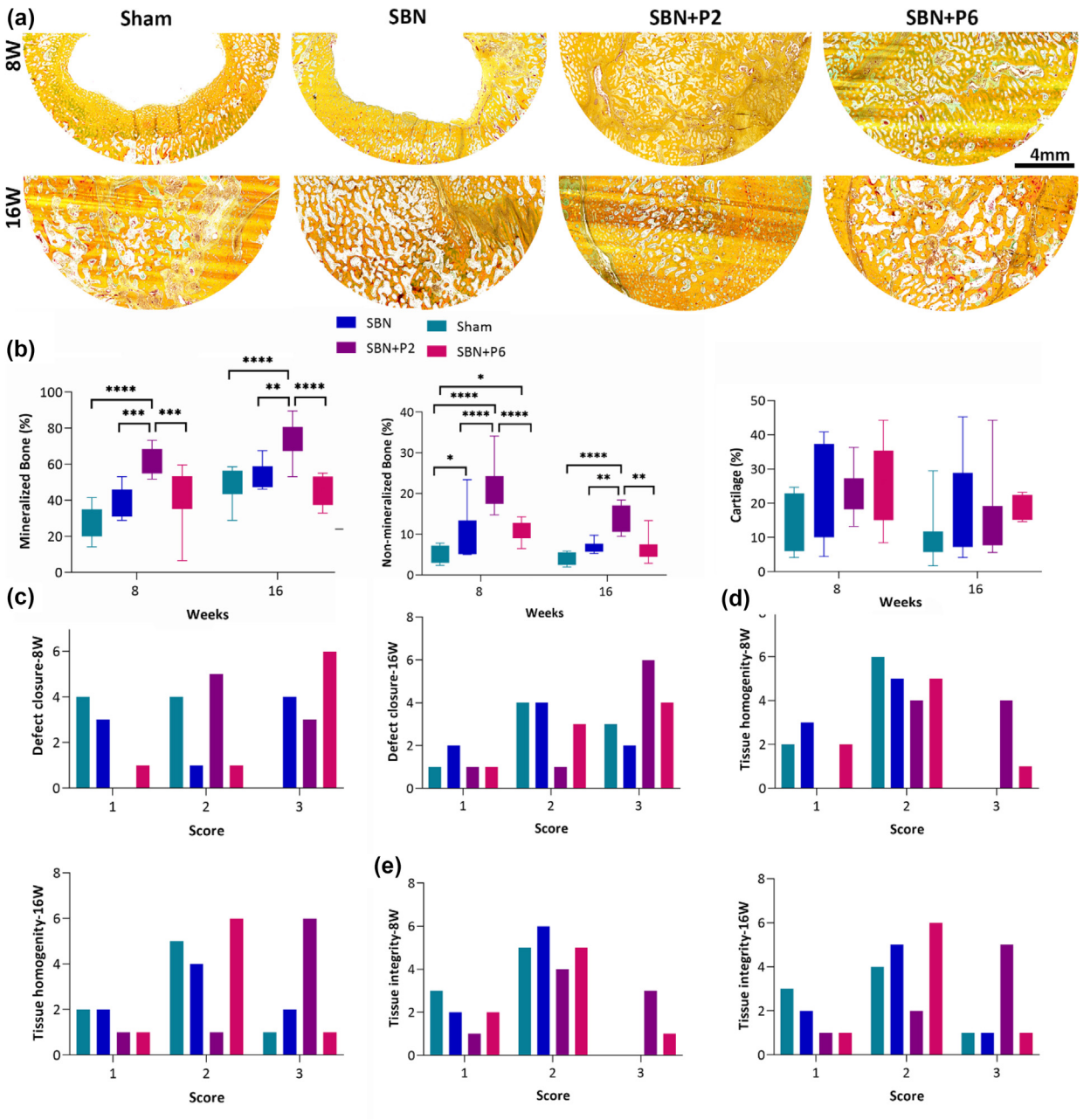

FIGURE 3

Studying bone and cartilage formation effects of proline-rich disordered peptides. (a) Representative images of Movat Pentachrome histology staining in four groups including sham, SmartBone® (SBN), SBN + P2 and SBN + P6. Mineralized and non-mineralized bone as well as cartilage formation were evaluated in all groups after 8 and 16 weeks of healing, (N = 8), scale bar = 4 mm. (b) Quantitative histomorphometrical data of mineralization, non-mineralization and cartilage distribution percentage using movat pentachrome histology staining. Significant differences were presented as *P < 0.05, **P < 0.01, ***P < 0.001 and ****P < 0.0001. (c-e) Descriptive analysis of defect closure (c) as well as tissue homogeneity (d) and integrity (e) in all groups using a 3-point scale system (good, fair, poor for 1 to 3, respectively) after 8 and 16 weeks of healing.

ples had good defect closure and tissue homogeneity (category 3), all SBN + P2 and SBN + P6 samples were in the fair and good categories (2&3). The difference was more evident after 16 weeks of healing, as the vast majority of the SBN + P2 samples were in the good category for all the three parameters, samples from other groups were mainly in the fair category. These data confirmed data obtained from quantitative histomorphometry analysis indicating the substantial influence of proline-rich disordered P2 in stimulating later osteogenesis and mineralization processes.

Immunohistochemistry

Using α-SMA positive blood vessels, we studied the blood vessel formation both quantitatively and descriptively in calcified samples. The quantitative data showed that the percentage of α-SMA positive blood vessels in the SBN + P2 was higher than other groups at both time points indicating higher blood vessel activities in this group (Fig. 4a). The α-SMA positive blood vessels in the SBN + P2 was significantly greater than the sham group, with P values of 0.0365 and 0.0197 after 8 and 16 weeks of healing, respectively. The blood vessel activity was the same in both sham

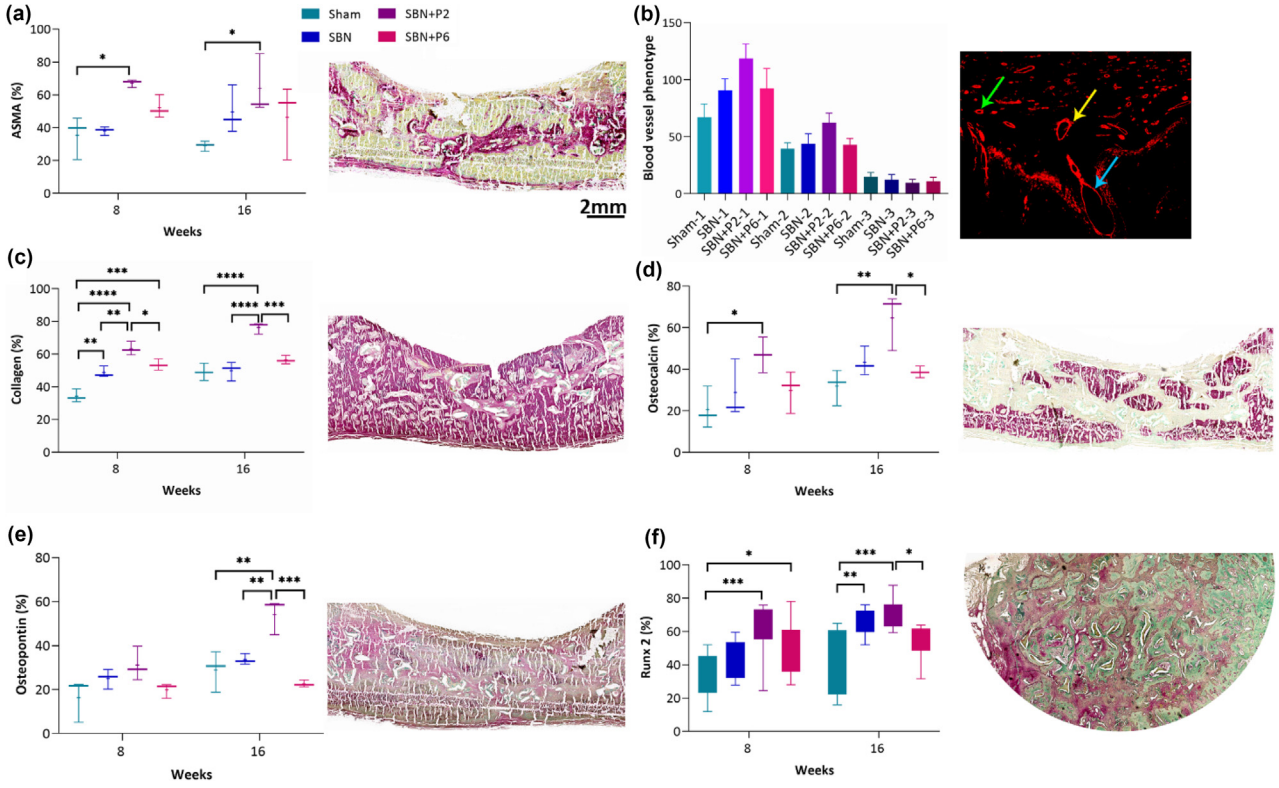

FIGURE 4

Immunohistochemical analysis of the effects of proline-rich disordered peptides on bone formation biological markers in four groups including sham, SmartBone® (SBN), SBN + P2 and SBN + P6. Quantitative data and representative images of alpha smooth muscle and Actin, α-SMA, $N = 3$, scale bar = 2 mm (a). Descriptive analysis and a representative fluorescent image of α-SMA antibody staining used for evaluating the blood vessel regularity over time using a 3-point scale system (b). The round shape vessels were categorized as regular type 1 vessels, green arrow, small to moderate oval shape ones as regular type 2, yellow arrow and big vessels in oval or other undefined shapes as irregular type 3 vessels, blue arrow (b). Quantitative data and representative images of collagen type I (c), osteocalcin (d), osteopontin (e), $N = 3$, and runt-related transcription factor 2, Runx 2, $N = 8$, (f) biological markers, scale bar = 1 mm. Significant differences were presented as $^{*}P < 0.05$, $^{**}P < 0.01$,$^{***}P < 0.001$ and $^{****}P < 0.0001$.

and SBN groups after 8 weeks of healing; however, it was higher for the SBN group than that of the sham after 16 weeks of healing, indicating the influences of SBN on late bone formation. Results from our descriptive analysis showed that although the percentage of blood vessels was higher in the SBN + P2, the majority of blood vessels had a regular phenotype for all groups independent on the time point (Fig. 4b).

Results from collagen type I antibody staining in the calcified samples showed significantly higher positive reaction in all treated groups compared to the sham after 8 weeks of healing with higher values for the peptide groups (Fig. 4c). After 16 weeks of healing, the SBN + P2 formed a significantly higher percentage of collagen type I than sham, SBN and SBN + P6 with P values of <0.0001, <0.0001 and 0.0001. In addition, this group had greater osteocalcin, osteopontin and RUNX 2 positive reactions than other groups at both time points (Fig. 4d–f). Although P2 showed its favorable influences on bone formation markers at both time points, P6 mainly affected the expression of bone formation markers at the earlier time point. In general, studying bone formation markers on both calcified and decalcified samples showed that both P2 and P6 could significantly influence bone formation and mineralization processes; however, they might have different mechanisms affecting bone formation. In addition, the RUNX 2 marker analysis in decalcified samples with a greater sample size showed significant differences between the SBN and sham groups, indicating the stimulatory effects of using SBN on bone formation.

Hydroxyapatite platelet properties

The bone ultrastructure was studied using synchrotron SAXS and XRD, which revealed platelet orientation and thickness (T) as well as crystal size and lattice spacing (d) of Hap, respectively [45]. In the following section, we first discuss the two-dimensional distribution of the T-parameter and the orientation of HAp determined by SAXS signals. Afterward, we will discuss the evolution of the crystallites as determined by XRD.

The sham group exhibited a low mineralization amount after 8 weeks of healing (Fig. 5a). In the center, where the defect was located, no scattering signal could be detected. However, after 16 weeks of healing, a massive bone formation occurred. The HAp platelet size, described by the T parameter, was homogenously distributed along with the defect position. The T parameter was only evaluated at the positions where a scattering signal was significantly strong. The orientation and degree of orientation were for both time points parallel to the bone, with an overall weak degree of orientation in the range of 5%. For more qualitative analysis, the T parameter distribution and orientation degree were plotted in a histogram (Fig. 5b–e). The histograms

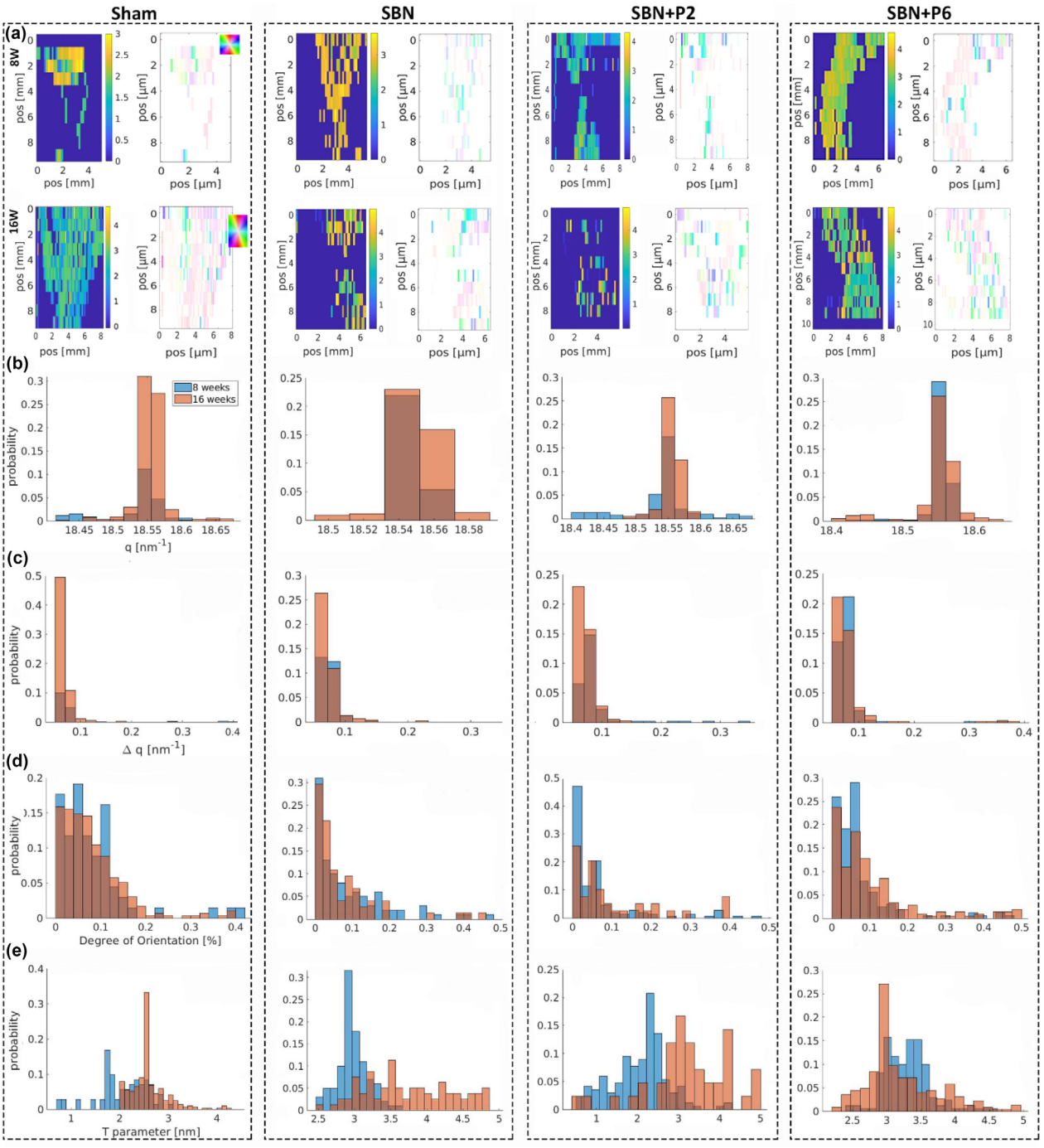

FIGURE 5

Small angle X-ray scattering/X-ray diffraction (SAXS/XRD) analysis of the osteogenesis and biomineralization processes after 8 and 16 weeks of healing. (a) Two dimensional maps showing the distribution of orientation and T parameter in four groups including sham, SmartBone® (SBN), SBN + P2 and SBN + P6. Histograms of the peak position of 002 HAp reflection (b), the fwhm 002 HAp reflection (c), the degree of orientation (d) and T parameter (e) of the defect site are shown in the top panel (a). The color wheel directly corresponds to the degree of orientation.

that describe the distribution of 2D map parameters showed no changes over time. The T parameter was shifted, having a broad distribution ranging from 1.5 to 3 nm after 8 weeks. However, after 16 weeks of healing, the distribution was narrower, centering around 2.7 nm. The crystal also was slightly affected by the healing time. The d-spacing distribution was broader after 8 weeks compared to that of 16 weeks healing time point; however, both histograms centered at the same value. The fwhm (full width at half maximum) was not affected by the healing time, suggesting the same crystallite size at both healing time points.

The overall mineralization amount was also low for the SBN. The two-dimensional maps of T parameter showed a uniform distribution of T parameter along with the bone sample at both healing time points (Fig. 5a). This group showed a week orientation parallel to the bone shaft. The histograms of the degree of orientation exhibited no differences between 8 and 16 weeks of

healing. The T-parameter centered around 3.1 nm; however, the distribution broadened significantly after 16 weeks of recovery (Fig. 5b–e).

In the SBN + P2 group, the T parameter showed that the mineralization for 8 and 16 weeks was very sparse with no homogenous distribution (Fig. 5a). The orientation and degree of orientation were also relatively low. The color wheel directly corresponds to the direction of orientation. The primary color is identified in green and red, showing an orientation parallel to the bone. The overall degree of orientation was also relatively low (Fig. 5b–e). No change in the degree of orientation could be identified as a function of healing time. This was different for the T-parameter. The T-parameter centers' distribution was around 2.5, with an increase to 3.2 after 16 weeks. The crystal structure of the HAp was distorted at the beginning showing a slight variation of the d-spacing. With an increase in healing time, d-spacing centered around 18.55 nm^{-1}. The fwhm of the 002-diffraction peak decreased slightly indicating a growth of the crystals as this parameter was directly influenced by the number of crystal planes with a decrease of the fwhm along with an increased number of lattice planes.

On the other hand, the SBN + P6 group had different features than other groups. Overall, more mineralization could be seen (Fig. 5a). The T-parameter was homogenously distributed in the healing region for both time points; however, the two-dimensional maps showed no time-dependent changes. As

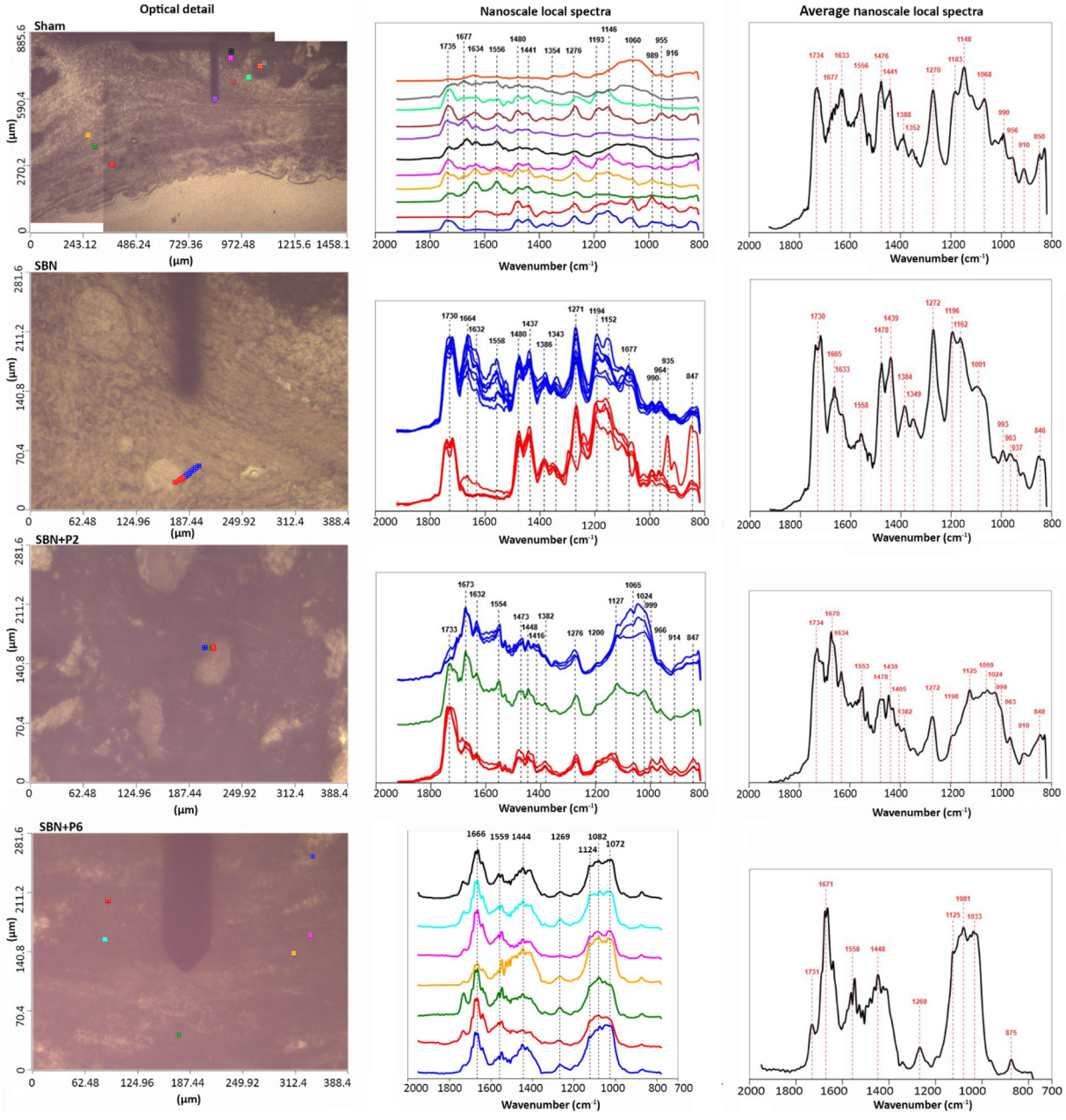

FIGURE 6

Representative images of location-specific nanoscale atomic force microscopy-infrared (AFM-IR) analysis. Optical and nanoscale local spectra detail of four groups: sham, SmartBone® (SBN), SBN + P2 and SBN + P6 after 8 weeks of healing.

indicated by the faint color, the orientation and its degree were also parallel to the bone shaft with a low degree of orientation at both healing time points. The degree of orientation was not time-dependent and could be considered constant. The T parameter showed a slight variation centering after 8 weeks, around 3.2 nm, decreasing to roughly 3 nm after 16 weeks. The XRD data indicating the crystal structure showed no significant differences in the d-spacing/crystal structure or fwhm and crystal size. These data indicated that the mineralized bone had the same structure in SBN + P6 group at both healing time points.

In summary, based on SAXS and XRD data, the treatment groups did not influence the degree of orientation and orientation of ultra-structures. The crystal structure of samples evaluated by XRD also was not significantly influenced with a d-spacing centering around 18.55 nm^{-1}.

On the other hand, the T parameter showed some variations depending on the treatment group. We should bear in mind that evaluated lattice planes in the stable fwhm are perpendicular to the long platelet axis. In contrast, the T parameter is sensitive to the thickness of platelets. Hence, in the SBN + P2 group, we observed a decrease in the overall size of T parameter, which is typical for healing bone as woven bone is known to have larger platelets that shrink down during maturation. However, we could not detect such an effect for the SBN + P6 group, while the histograms centered on the same value with a slight shift to larger values after 8 weeks of healing. In addition, such behavior could not be seen for the sham and SBN groups. The SBN group showed a T parameter distribution around 3 nm, which could indicate an already healed defect site. However, after 16 weeks of healing, the histogram was significantly broadened and shifted to the platelet size. For the sham group, the T parameter distribution was also quite broad and centered at lower T parameter values at around 2.8 nm and we observed lower mineralization amount at the earlier stages of healing.

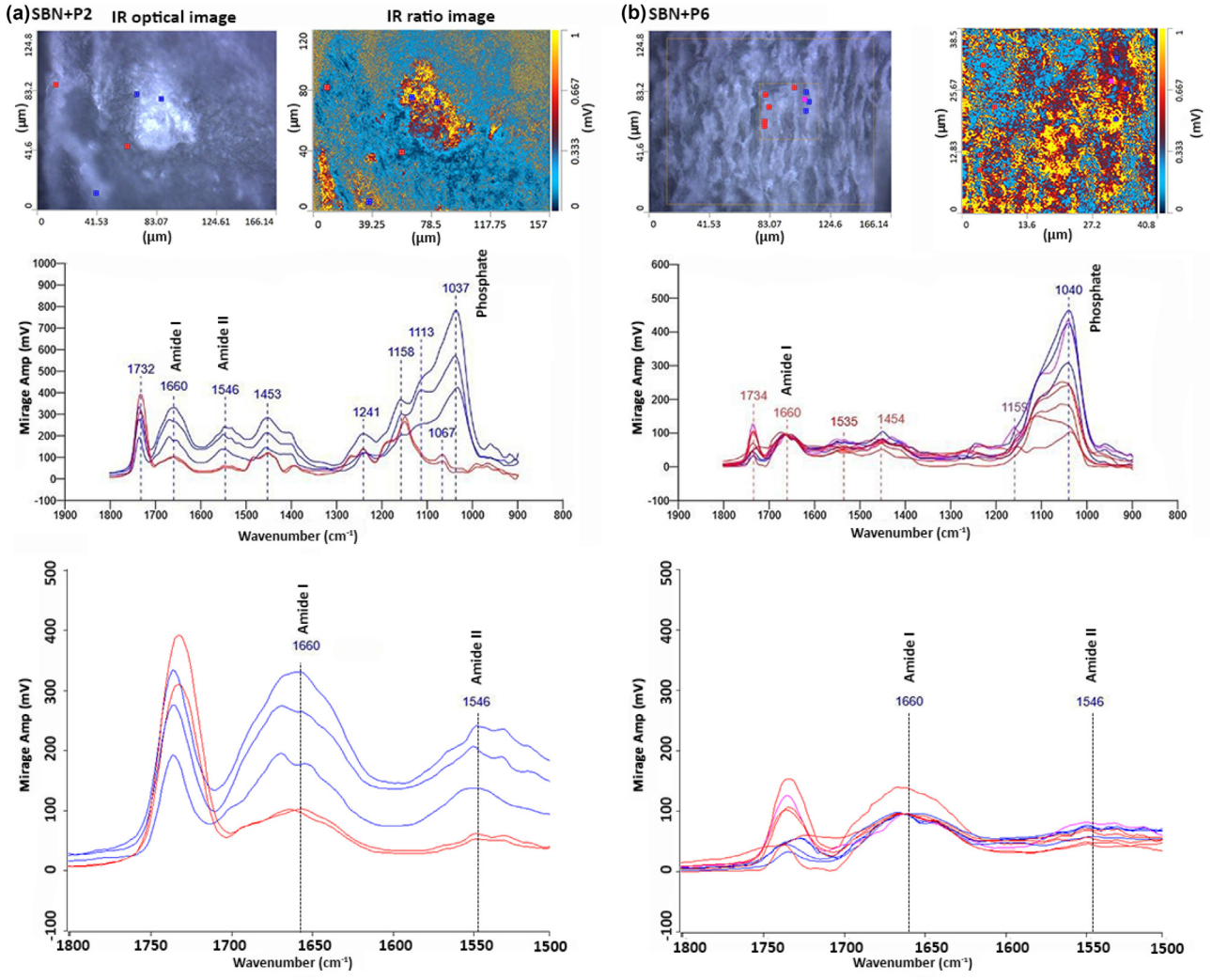

FIGURE 7

Studying the osteogenesis and biomineralization effects and conformational changes of peptides using optical photothermal IR (O-PTIR) microscopy. Markers on the IR 40× optical image indicate the location of subsequent IR spectra. The ratio of two single-frequency images (1037/1660 cm^{-1}), which highlights the regions rich in mineral and amine content we observed in the spectra, were also shown in IR ratio image.

Topographical and chemical differences using AFM-IR and O-PTIR

Studying the chemical properties of newly formed bone matrix at high resolution plays key roles in understanding the effects of biomaterials on tissue healing mechanisms [46]. Recent efforts have led to developing AFM-IR and O-PTIR as new techniques for high-resolution imaging of materials beyond optical microscopy's diffraction-limited resolution [47]. Therefore, we studied the potential of these techniques in evaluating the healing effects of designed biomaterials on calcified bone sections. We firstly used AFM-IR, which can resolve vibrational mode variations in 100 nm features. The technique combines atomic force microscopy with photothermal infrared deflection spectroscopy to study topography and chemical structure of materials [47]. However, because of the influence of sectioning microtome on the sectioned samples, studying the surface roughness changes between the groups was challenging in this study. Hence, we only focused on the chemical differences between the groups using the two mentioned techniques. To study the effects of disordered peptides on biomineralization, we studied the distribution of phosphate (PO_4^{3-}) and amide (N–H) primary and secondary bonds showing at 1030–1080, 1660 and 1546 cm^{-1}, respectively (Fig. 6). Despite the sham group, we could detect strong PO_4^{3-} and N–H primary and secondary stretching in the treated groups, with apparent changes of N–H primary IR absorbance peak after encapsulating P2 and P6 into the SBN, verifying their release into the defect area. In addition, PO_4^{3-} peak was more stretched in peptide groups compared to the SBN. Although this technique could provide us some information about the chemical structure of samples, it has some limitations, including the difficulties of AFM tip-sample interactions and time consuming for high-resolution scans [47]. Consequently, we used O-PTIR technique to evaluate the effects of peptides on osteogenesis and biomineralization in detail.

Using O-PTIR as a non-contact chemical technique, we could evaluate the conformational changes of peptides and their effects on osteogenesis and biomineralization in detail (Fig. 7). In this technique, a visible light probe laser detects the selective absorbance of mid-IR excitation laser light through a photothermally induced thermal lensing, achieving sub-micron IR spectra using non-contact technique and independent on surface roughness [47]. High resolution IR optical and ratio images were collected at different spots of the SBN + P2 and SBN + P6 groups to visualize the distribution of phosphate and amide moieties. The IR spectra results showed a prominent IR absorbance band at 1037 cm^{-1} confirming the stimulatory effects of peptides on bone formation and biomineralization processes. The strong stretching of amide primary and secondary IR absorbance peaks at 1660 and 1546 cm^{-1} in the SBN + P2 group verified that this peptide experienced more conformational changes after implantation with a higher phosphate intensity at 1037 cm^{-1}, which led to a better bone formation of the defect site compared to peptide 6 (Figs. 7&S13). These results also highlighted the potential of using O-PTIR technique as a valuable tool in evaluating the effects of implanted biomaterials and conformational changes of peptides on bone healing at high resolutions. The O-PTIR also has a complementary Raman microscopy system; however, due to the auto-florescence of PMMA, we could not detect any meaningful spectra using Raman peaks (data not shown).

Discussion and conclusion

This study demonstrates the potential of designed proline-rich IDPs as candidates for enhancing bone healing and biomineralization in clinical applications. Our *in vitro* studies exhibited a significantly higher amount of ALP activity as well as *osteocalcin* and *collagen type I* gene expression in the SBN + P2 and SBN + P6 compared to EMD. In addition, the SBN + P2 and SBN + P6 had significantly higher osteoprotegerin and osteopontin protein expression compared to the SBN group [26]. Because the designed peptides improved the expression of bone formation markers *in vitro* [26,27], the *in vivo* testing of the composites was favorable. The careful choice of appropriate animal models and suitable imaging technologies are crucial in evaluating biomaterials *in vivo* [48]. This study utilized the pig craniotomy model because of its biological and physiological advantages over small animal models [49]. Moreover, in light of a possible clinical translation, we chose a skeletally immature model, a more complex but more realistic test bench for bone grafts aiming to challenge bone defect regeneration. We investigated the healing progression using various imaging techniques to reflect the clinical outcomes.

Indeed, the results reflected an improvement of new bone formation after 8 and 16 weeks of healing in the experimental groups. This finding indicates an increased osteoinductive capacity resulting from encapsulating IDPs into the mineralized bone matrix graft. The enhancement of the healing progression was also reflected on the matrix mineralization examined histologically and using SAXS/XRD, FLARE and O-PTIR. These results are in accordance with the histomorpholometrical results of cellular and extracellular matrix markers, which showed enhanced catabolic activity in the presence of the IDPs.

Although both developed IDPs had very similar chemical structures, we detected different conformational changes and biomineralization effects in both groups in our *in silico* and *in vivo* experiments. Our *in silico* studies demonstrated that P2 was more thermodynamically stable than P6. P2 showed an ability for faster spontaneous folding and conformational changes than P6 under both OPLS-AA/L-TIP3P and OPLSIDPSFF-TIP4P-D + PBS conditions during the simulated timescale up to 1000 ns. Although OPLS-AA/L-TIP3P is more commonly used for simulating peptides, we observed that OPLSIDPSFF-TIP4P-D + PBS condition was more favorable for IDPs molecular simulations, which was in accordance with the findings of Yang et al. [29] study.

Our *in vivo* studies demonstrated that the resulting conformational changes of the SBN + P2 contributed to a better bone tissue mineralization than the SBN + P6 group. In contrast, the SBN + P6 had a favorable influence on cartilaginous tissue and non-mineralized tissue formation compared to the SBN + 2 group. These changes could be because of the presence of serine as a polar amino acid in P2 (Fig. S4), which is known to enhance the mineralization of the dentin ECM [50].

Furthermore, osteopontin, as a key player in directing bone formation processes, is a serine-rich glycol-phosphoprotein. Lin et al. [51] demonstrated that serine amino acid is essential for the survival stimulatory effect of osteopontin [51]. In an effort to mimic the properties of osteopontin, Salgado et al. [52] studied the effects of a phosphorylated amino acid (O-phospho-L-serine) on enhancing the bone regeneration potential of nanohydroxyapatite and collagen-based composite materials [52]. Their results exhibited that the serine-rich scaffolds could enhance the differentiation of human MSCs, cell viability and bone tissue ECM production *in vitro* and *in vivo* [52]. Hence, the more substantial effects of P2 on biomineralization compared to P6 could be because of the presence of serine amino acid and its stimulatory roles on osteopontin. Since osteopontin is a multifunctional molecule with both structural and humoral activities [53], we believe that P2 might affect bone formation by affecting osteopontin functions.

This study employed O-PTIR and FLARE techniques chemical tools, for the first time, to evaluate the bone-biomaterial interactions at high resolutions. Thereby, the histological and radiological results were inferred through the distinctive recognition between mineralized and non-mineralized bone tissue using carbohydrate- and amine-reactive covalent stains, respectively. The results accord with the osteoid-specific Von Kossa/Van Gieson staining. O-PTIR and FLARE have high potentials and can serve as complementary techniques for histological and immunohistochemical evaluations of bone tissue. However, further chemical probes should be developed to study the detailed structure and signaling pathways of osteogenesis and biomineralization using FLARE.

In addition, our SAXS and XRD data provided us detail information on how IDPs affected the distribution, orientation and size of HAp in different ways, which are consistent with our histology data. Using AFM-IR and O-PTIR, we could confirm the changes in phosphate and amide chemical bands in treated groups showing the effects of peptides on osteogenesis and biomineralization. Although AFM-IR could provide some general information about the differences between groups, we could detect the conformational changes of peptides and their influences on the intensity of amide bands only after using O-PTIR. The observed spontaneous folding and conformational changes of P2 in MD analysis are consistent with the O-PTIR results. Since O-PTIR collects spectra in laser-induced reflection mode thickness, surface roughness or particle shape/size were not complicating issues as opposed to AFM-IR. If the histological slides were deplasticized, further information could have been obtained with the combined Raman microscope, as PMMA interfered with the Raman signal. These data supported using O-PTIR technique as a strong chemical tool for evaluating the bone regeneration potential of biomaterials and conformational changes of IDPs after implantation.

Taken together, using the IDPs could be beneficial for stimulating early and late bone healing and biomineralization processes in bone xenograft composites used in critical size skeletal defects. The SBN + P6 could be more convenient for medical indications, where cartilaginous tissue and early bone formation are more critical than late biomineralization as in the case of osteoporotic patients. While SBN + P2 is more beneficial in indications where late bone formation and biomineralization are more crucial than bone healing than in diabetic patients. This study shows that the innovative biomaterials shall be examined in-depth using an interdisciplinary methodology. The novel techniques used here, for the first time, hold promises for an essential improvement in the analysis and diagnosis of bone and bone–biomaterial interface.

Declaration of Competing Interest

The authors declare that they have no known competing financial interests or personal relationships that could have appeared to influence the work reported in this paper.

Acknowledgments

This work was supported by a project “Promoting patient safety by a novel combination of imaging technologies for biodegradable magnesium implants, MgSafe” funded by European Training Network within the framework of Horizon 2020 Marie Skłodowska-Curie Action (MSCA) grant number No 811226 (www.mgsafe.eu). Joshua C. Vaughan acknowledges support from NIH grant R01 MH115767. This study acknowledges the Eureka Eurostars Project -E!9624 ‘Bio-hybrid composite bone graft for paediatric bone regeneration’ http://www.smartbonepep.eu/. Histological images were acquired at the Norbrain Slide scanning Facility at the Institute of Basic Medical Sciences, University of Oslo, a resource funded by the Research Council of Norway. Dr. Liebert Nogueira is kindly acknowledged for assistance with micro-CT scans and data processing. Mrs. Annette Stengel and Mr. Mohammad El Khassawna at the Experimental Trauma Surgery, Justus-Liebig University Giessen, Giessen, Germany are also acknowledged for their assistance during the experiments. Hartmut Stadler and Miriam Unger, Bruker Nano Surfaces Division are acknowledged for conducting the AFM-IR analysis. Antti Kalanti, Bruker Nano Surfaces Division, is acknowledged for access to O-PTIR and AFM-IR. We acknowledge technical support by the SPC facility at EMBL Hamburg.

Competing interests

The authors declare no financial and personal relationships with other people or organizations that could inappropriately influence bias to this work. The rights for SmartBone® and SmartBonePep® patents and trademarks belong to Industrie Biomediche Insubri S.A. (Switzerland). Giuseppe Perale is a founding shareholder and the executive vice president of Industrie Biomediche Insubri S.A. (Switzerland), the company that fully owns all IPRs (US Patent US8367602B2, PCT/IB2007/004068, EP Patent EP2358407B1 and related bundles) on SmartBone® and SmartBonePep® and their trademarks.

Author contribution statements

GP, SPL and HJH conceived the project. MR carried out the experiments. HJH, SS, TEK and JCV supervised the study. AC and SPL conducted the animal study. CM and AA conducted the FLARE analysis. KI and FW collected and analyzed the SAXS and XRD analysis. ED conducted the O-PTIR analysis. MR and HJH wrote the manuscript with input from all authors.

Appendix A. Supplementary data

Supplementary data to this article can be found online at https://doi.org/10.1016/j.mattod.2021.12.001.

References

[1] S. Elsharkawy et al., Nat. Commun. 9 (2018), https://doi.org/10.1038/s41467-018-04319-0.
[2] N. Reznikov, R. Shahar, S. Weiner, Acta Biomater. 10 (2014) 3815–3826.
[3] Y. Liu et al., Adv. Mater. 28 (2016) 8740–8748.
[4] L. Addadi, S. Weiner, Angew. Chem., Int. Ed. Engl. 31 (1992) 153–169.
[5] P.E. Wright, H.J. Dyson, Nat. Rev. Mol. Cell Biol. 16 (2015) 18–29.
[6] A.L. Boskey, E. Villarreal-Ramirez, Matrix Biol. 52-54 (2016) 43–59.
[7] M. Wojtas, P. Dobryszycki, A. Ożyhar, IntechOpen (2012).
[8] F.G. Quiroz, A. Chilkoti, Nat. Mater. 14 (2015) 1164–1171.
[9] J. Liu et al., Biochemistry 45 (2006) 6873–6888.
[10] C.A. Galea et al., Biochemistry 47 (2008) 7598–7609.
[11] A. Kumar et al., Chem. Mater. 32 (2020) 8845–8859.
[12] K. Delak et al., Biochemistry 48 (2009) 2272–2281.
[13] Y. Yamakoshi, J.P. Simmer, Japanese Dental Sci. Rev. 54 (2018) 183–196.
[14] S. Lenton et al., Biophys. J . 112 (2017) 1586–1596.
[15] L. Kalmar et al., Bone 51 (2012) 528–534.
[16] F.M. Rubert, On the Role and Potential Use of Proline-rich Peptides in Bone Regeneration, University of Balearic Island, 2012. PhD thesis.
[17] M. Rubert et al., J. Biomater. Tissue Eng. 1 (2011) 198–209.
[18] J. Hatakeyama et al., J. Dent. Res. 88 (2009) 318–322.
[19] L. Biedermannova et al., PCCP 10 (2008) 6350, https://doi.org/10.1039/b805087b.
[20] Lyngstadaas SP, Ellingsen JE, inventors;. Consensus peptide. 2008 PCT/WIPO Patent Number WO2008078167A2.
[21] J.M. Ramis et al., Tissue Eng. Part A 18 (2012) 1253–1263.
[22] M.L. Azi et al., BMC Musculoskeletal Disorders. 17 (2016) 1–10.
[23] Y. Fillingham, J. Jacobs, Bone Joint J. 98-B (2016) 6–9.
[24] S.M. Meloni et al., Eur. J. Oral Implantol. 10 (2017) 425–432.
[25] C.M. Schmitt et al., Clin. Oral Implant Res. 26 (2015) 1043–1050.
[26] H. Zhu et al., ACS Appl. Bio Mater. 3 (2020) 2263–2274.
[27] H. Zhu et al., Front. Cell Dev. Biol. 8 (2020) 1617.
[28] W. Jorgensen et al., J. Chem. Phys. 79 (1983) 926–935.
[29] S. Yang et al., J. Chem. Inf. Model. 59 (2019) 4793–4805.
[30] V.B. Chen et al., Acta Crystallogr. D Biol. Crystallogr. 66 (2010) 12–21.
[31] A. Cingolani et al., Curr. Pharm. Biotechnol. 19 (2019) 1005–1013.
[32] D. D'Alessandro et al., Int. J. Pharm. 523 (2017) 534–544.
[33] G. Perale et al., J. Clin. Med. 8 (2019) 2159.
[34] H.Z. Movat, AMA Arch. Pathol. 60 (1955) 289.
[35] Leung K-S, Qin L, Cheung WH. A practical manual for musculoskeletal research: World Scientific; 2008.
[36] T. El Khassawna et al., PLoS ONE 8 (2013) e71665.
[37] C. Schlundt et al., Bone 106 (2018) 78–89.
[38] U. Thormann et al., Biomaterials 34 (2013) 8589–8598.
[39] C. Mao et al., Sci. Adv. 6 (2020) eaba4542.
[40] D.E.S. Daghma et al., J. Bone Miner. Metab. 36 (2018) 297–306.
[41] D. Malhan et al., Front. Endocrinol. 9 (2018) 666.
[42] A. Gourrier et al., J. Appl. Crystallogr. 43 (2010) 1385–1392.
[43] O. Glatter, O. Kratky, Small angle X-ray scattering, UK, Academic press, London, 1982.
[44] J. Henriques, J. Mol. Biol. 430 (2018) 2521–2539.
[45] B. Zeller-Plumhoff et al., Acta Biomater. 101 (2020) 637–645.
[46] J. Horne et al., Adv. Mater. Interfaces 7 (2020) 1901851.
[47] A.J. Wang et al., Adv. Mater. Interfaces 8 (2021) 2001720.
[48] M. Rahmati et al., Chem. Soc. Rev. 49 (2020) 5178–5224.
[49] A.I. Pearce et al., Eur. Cells Mater. 13 (2007) 1–10.
[50] D.K. Yarbrough et al., Calcif. Tissue Int. 86 (2010) 58–66.
[51] Y.-H. Lin, H.-F. Yang-Yen, J. Biol. Chem. 276 (2001) 46024–46030.
[52] C.L. Salgado, B.I.B. Teixeira, F.J.M. Monteiro, Front. Bioeng. Biotechnol. 7 (2019) 206.
[53] J. Si et al., Med. Sci. Monit. 26 (2020) e919159–e919161.